

Low voltage drop tunnel junctions grown monolithically by MOCVD

Cite as: Appl. Phys. Lett. **118**, 053503 (2021); <https://doi.org/10.1063/5.0033554>

Submitted: 16 October 2020 . Accepted: 07 January 2021 . Published Online: 02 February 2021

 Zane Jamal-Eddine,  Syed M. N. Hasan,  Brendan Gunning,  Hareesh Chandrasekar,  Mary Crawford,  Andrew Armstrong,  Shamsul Arafin, and Siddharth Rajan



View Online



Export Citation



CrossMark



Your Qubits. Measured.

Meet the next generation of quantum analyzers

- Readout for up to 64 qubits
- Operation at up to 8.5 GHz, mixer-calibration-free
- Signal optimization with minimal latency

Find out more



Low voltage drop tunnel junctions grown monolithically by MOCVD

Cite as: Appl. Phys. Lett. **118**, 053503 (2021); doi: [10.1063/5.0033554](https://doi.org/10.1063/5.0033554)

Submitted: 16 October 2020 · Accepted: 7 January 2021 ·

Published Online: 2 February 2021



View Online



Export Citation



CrossMark

Zane Jamal-Eddine,^{1,a)} Syed M. N. Hasan,¹ Brendan Cunning,² Hareesh Chandrasekar,¹ Mary Crawford,² Andrew Armstrong,² Shamsul Arafin,¹ and Siddharth Rajan^{1,3}

AFFILIATIONS

¹Department of Electrical and Computer Engineering, The Ohio State University, Columbus, Ohio 43210, USA

²Sandia National Laboratories, Albuquerque, New Mexico 87185, USA

³Department of Materials Science and Engineering, The Ohio State University, Columbus, Ohio 43210, USA

^{a)} Author to whom correspondence should be addressed: jamal-eddine.1@osu.edu

ABSTRACT

Tunnel junction devices grown monolithically by metal organic chemical vapor deposition were optimized for minimization of the tunnel junction voltage drop. Two device structures were studied: an all-GaN homojunction tunnel junction and a graded InGaN heterojunction-based tunnel junction. This work reports a record-low voltage drop in the graded-InGaN heterojunction based tunnel junction device structure achieving a de-embedded tunnel junction voltage drop of 0.17 V at 100 A/cm². The experimental data were compared with a theoretical model developed through technology computer-aided design (TCAD) simulations that offer a physics-based approach to understanding the key components of the design space, which lead to a more efficient tunnel junction.

Published under license by AIP Publishing. <https://doi.org/10.1063/5.0033554>

There has been significant interest recently in the study of III-nitride tunnel junction-enabled optoelectronic devices. It has been demonstrated that tunnel junctions can enable a variety of novel device structures to address some of the major issues faced by the community. Tunnel junctions find applications for current spreading into p-GaN layers without the need for absorbing ITO contacts^{1,2} and for improved hole injection efficiency into ultraviolet light emitting diodes (UV-LEDs).^{3–7} Tunnel junctions can also be utilized to cascade multiple light emitting diode (LED) active regions, which enable a significant increase in external quantum efficiency (EQE),^{8–11} and calculations have shown that the tunnel junction enabled cascaded multi-active region LED device structure supports the possibility of an EQE exceeding 100%.^{8,12,13} The multi-junction cascaded LED structure enables high output power while operating in a low current density regime. This is accomplished by operating at a higher voltage, which is sufficient to bias the multiple active regions within the device. By operating at lower current densities where the LEDs do not suffer from efficiency droop, it is possible to improve wall-plug efficiency. It is critical to have a low tunnel junction voltage drop for the cascaded multi-junction structure to improve wall-plug efficiency at high-output power operation. LED active regions of different emission wavelengths can also be cascaded to achieve multi-peak emission spectra.^{14–16} Beyond LEDs, tunnel junctions also improve performance in edge-

emitting and vertical-cavity lasers.^{17–22} With potential to address issues such as current spreading, injection efficiency to UV emitters, and efficiency droop mitigation, as well as to enable novel device structures, it is critical to reduce tunnel junction voltage losses to enable high-performance III-nitride optoelectronic devices.

Previous work on tunnel junctions employed a variety of growth techniques, including MBE,^{17,23–27} metal organic chemical vapor deposition (MOCVD),^{21,28–33} and hybrid (MOCVD + MBE).³⁴ The tunnel junctions with the lowest voltage drop to date have been reported by MBE growth^{35–38} because MOCVD-grown tunnel junctions have faced doping issues that increase resistivity and voltage drop. Limitations on maximum doping densities associated with MOCVD growth alongside the memory effect present in magnesium doped layers grown by MOCVD have led to tunnel junctions with higher voltage penalties than their MBE-grown counterparts. Hybrid growth techniques have addressed some of the issues innate to MOCVD-grown tunnel junctions, reducing the voltage drop across the tunnel junctions grown by this method, while still offering the ability to grow the active region of the LED or laser diode by MOCVD. However, the hybrid growth technique still introduces extra steps in the growth process, which increase process complexity and cost. There is significant motivation for improving the efficiency of tunnel junctions grown monolithically by MOCVD since this growth method can

provide the most manufacturable active regions. In this work, we report state-of-art tunnel junction voltage drop in MOCVD-grown tunnel junction device structures designed to mitigate doping limitations inherent to MOCVD growth. We develop a detailed model to understand the characteristics of tunnel junctions, which can help guide future tunnel junction design for MOCVD-grown structures.

The epitaxial structures investigated here are shown in Fig. 1. MOCVD growth was performed at atmospheric pressure in a Taiyo Nippon Sanso SR4000HT reactor. The substrates were $\sim 6 \mu\text{m}$ thick n-type GaN/sapphire c-plane templates with a typical dislocation density of $\sim 10^8 \text{ cm}^{-2}$. For the p-n junction structures, the n-type and p-type layers were grown at 1050°C and 1015°C , respectively. The tunnel junction layers, including the $\sim 450 \text{ nm}$ thick n-GaN layer, were grown at reduced temperatures (compared to the p-n junctions) of $900\text{--}975^\circ\text{C}$ in order to reduce the thermal budget. The growth temperatures in the tunnel junction layers are typical for GaN layers in standard GaN LED growth. The graded InGaN layers in the heterojunction based tunnel junction structures were grown at 830°C .

The three samples we discuss here include a reference p-n diode with a metal/p+ contact, a p-n junction with an n+/p+ tunnel junction, and a p-n junction with a graded InGaN-based tunnel junction. The standalone p-n diode structure [Fig. 1(a)] was grown on a $6 \mu\text{m}$ thick n+GaN sapphire template with $[\text{Si}] = 5 \times 10^{18} \text{ cm}^{-3}$, followed by

a 500 nm thick n+GaN bottom contact layer with $[\text{Si}] = 5 \times 10^{18} \text{ cm}^{-3}$, a 200 nm thick n-GaN layer with $[\text{Si}] = 2 \times 10^{16} \text{ cm}^{-3}$, and finally a 90 nm thick p-GaN layer with $[\text{Mg}] = 3 \times 10^{19} \text{ cm}^{-3}$. NPN structures were grown starting with the same p-n diode reference structure followed by a tunnel junction structure. It has been shown by Vadiee *et al.* that magnesium δ -doping can offer a significant reduction in the voltage penalty of GaN homojunction tunnel junction devices grown by MBE.³⁹ The GaN homojunction tunnel junction NPN structure consists of the reference p-n diode, followed by a magnesium delta-dose doping equivalent to $4.5 \times 10^{13} \text{ cm}^{-2}$ inserted at the beginning of the p++GaN layer of the tunnel junction as indicated by the red line in Fig. 1(b). Then, a 12 nm p++GaN layer with $[\text{Mg}] = 1.2 \times 10^{20} \text{ cm}^{-3}$ was grown to form the p-side of the tunnel junction. Next, a 6 nm n++GaN layer with $[\text{Si}] = 2.8 \times 10^{20} \text{ cm}^{-3}$ was grown to form the n-side of the tunnel junction. Figure 1(b) denotes the tunnel junction portion of the NPN structure with a black box. Finally, a 450 nm thick n+GaN recovery layer with $[\text{Si}] = 5 \times 10^{18} \text{ cm}^{-3}$ was grown to recover the smooth surface morphology after slight roughening in the heavily doped tunnel junction growth and serves as the top contact to the NPN device. The graded InGaN heterojunction tunnel junction NPN structure consists of the same p-n diode, followed by a magnesium delta-dose doping equivalent to $4.5 \times 10^{13} \text{ cm}^{-2}$ inserted at the beginning of the p++GaN layer of the tunnel junction as indicated by the red line in Fig. 1(c). Then, a

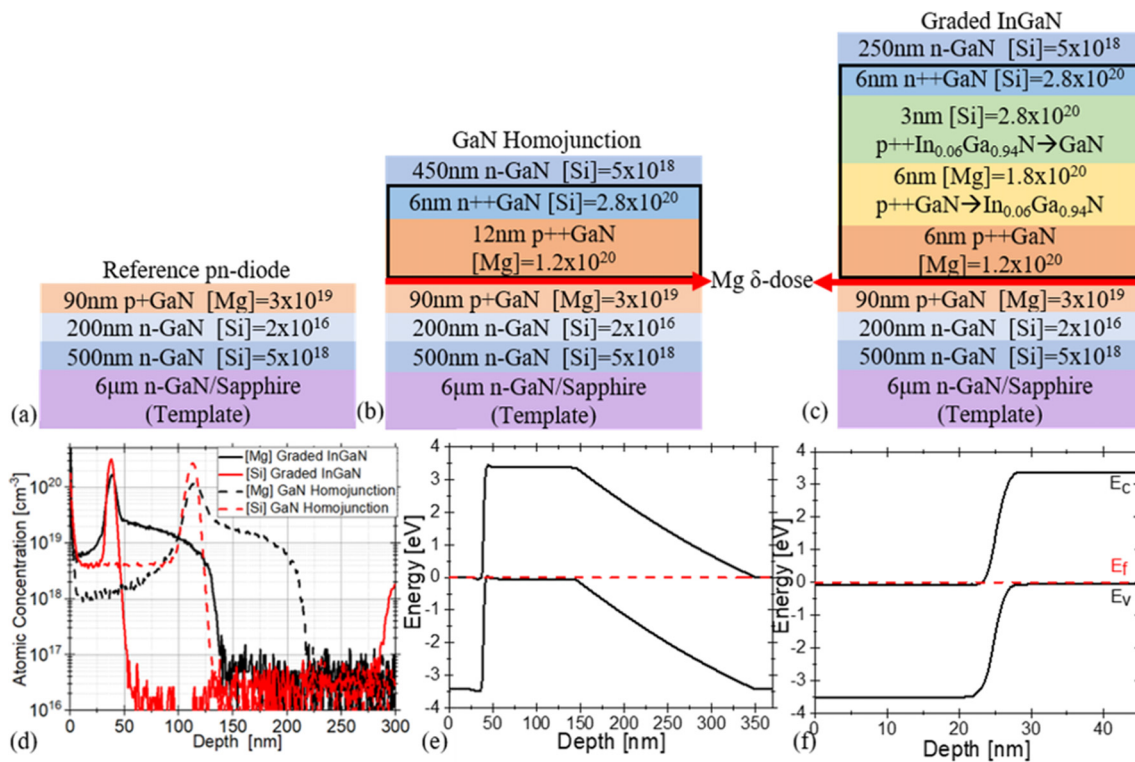


FIG. 1. The epitaxial structure of (a) the reference p-n diode structure, (b) a n-type, p-type, n-type (NPN) structure with a GaN homojunction tunnel junction (outlined in black) with Mg delta-dose grown on top of the reference p-n diode (GaN homojunction), and (c) a NPN structure with a graded InGaN heterostructure tunnel junction (outlined in black) with Mg delta-dose. (d) The Mg (black) and Si (red) doping concentrations as measured by SIMS for the graded InGaN heterojunction based tunnel junction (solid lines) and for the GaN homojunction tunnel junction (dashed lines). The Mg and Si profiles overlap due to the memory effect associated with MOCVD growth of Mg doped p-(In)GaN. (e) Energy band diagram for the full NPN structure with the graded InGaN heterojunction based tunnel junction. (f) Energy band diagram for the graded InGaN based tunnel junction.

6 nm p++GaN layer with $[Mg] = 1.2 \times 10^{20} \text{ cm}^{-3}$ was grown to form the p-side of the tunnel junction. Then, a 6 nm thick p++ graded InGaN interlayer with $[Mg] = 1.8 \times 10^{20} \text{ cm}^{-3}$ was grown graded from GaN at the bottom of the layer to $\text{In}_{0.07}\text{Ga}_{0.93}\text{N}$ at the top of the layer. Next, a 3 nm thick n++ graded InGaN interlayer with $[\text{Si}] = 2.8 \times 10^{20} \text{ cm}^{-3}$ was grown graded from $\text{In}_{0.07}\text{Ga}_{0.93}\text{N}$ at the bottom of the layer to GaN at the top of the layer. Then, a 6 nm n++GaN layer with $[\text{Si}] = 2.8 \times 10^{20} \text{ cm}^{-3}$ was grown. Figure 1(c) denotes the tunnel junction portion of the NPN structure with a black box. Finally, a 250 nm thick n+GaN recovery layer was grown with $[\text{Si}] = 5 \times 10^{18} \text{ cm}^{-3}$ was grown. The recovery layer thickness was reduced to 250 nm in the graded InGaN tunnel junction in order to limit the time that the InGaN layers were exposed to high temperature during the growth of subsequent layers.

All devices were fabricated starting with inductively coupled plasma reactive-ion etching (ICP-RIE) mesa-isolation followed by activation of buried p-GaN layers in a rapid thermal anneal system at 900°C for 30 min in N_2 ambient. The details of our optimized process for activation of MOCVD grown buried p-type layers are reported elsewhere.⁴⁰ Ti/Al/Ni/Au (20/120/30/50 nm) bottom contacts were, then, deposited and annealed at 850°C for 30 s in N_2 ambient. Finally,

full metal coverage top contacts composed of Al/Ni/Au (30/30/150 nm) and Pd/Ni/Au (30/30/30 nm) were deposited for the NPN and standalone p-n diode structures, respectively.

We combined delta-dose doping enhancement in the p++ tunnel junction layers with graded InGaN interlayers to achieve strong polarization-enhanced electric fields for increased tunneling probability. Takasuka *et al.* have previously shown that the introduction of graded InGaN layers with indium mole fractions up to $x = 0.4$ within the MOCVD grown tunnel junction can offer a significant improvement in tunnel junction efficiency.⁴¹ However, higher indium compositions also cause absorption losses within the InGaN layers. Therefore, we designed tunnel junctions with a maximum indium mole fraction of $x = 0.07$ as estimated by the SIMS measurement [Fig. 1(d)]. By limiting the indium content of the graded InGaN layers within the tunnel junctions to be significantly lower than those found in blue-violet emitter active regions ($x \geq 0.15$), we can limit absorption losses within the tunnel junction. The energy band diagram for the entire NPN structure with a graded InGaN interlayer tunnel junction is shown in Fig. 1(e), and the band diagram for just the graded InGaN interlayer tunnel junction is shown in Fig. 1(f).

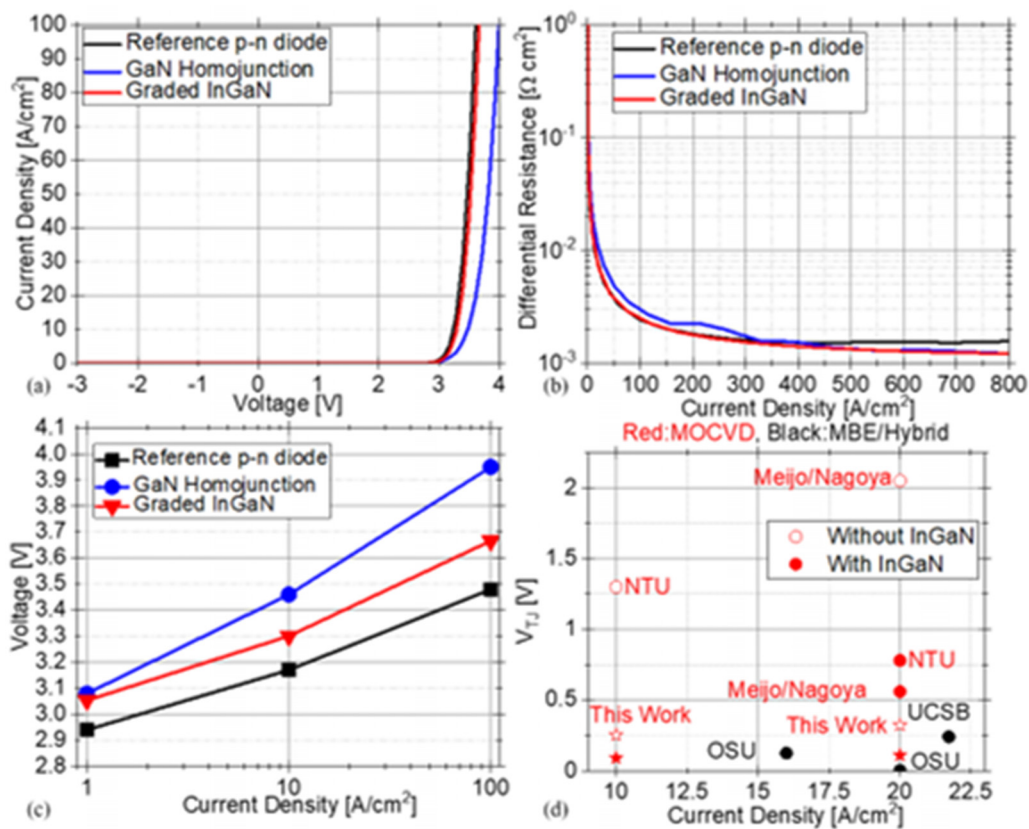


FIG. 2. (a) The measured current voltage characteristics for the reference p-n diode (black), the NPN structure with the GaN homojunction tunnel junction grown on top of the reference p-n diode (blue), and the NPN structure with the graded InGaN heterojunction tunnel junction (red). (b) Differential resistance vs current density for different device structures. (c) Voltage drop across the various devices at $1 \text{ A}/\text{cm}^2$, $10 \text{ A}/\text{cm}^2$, and $100 \text{ A}/\text{cm}^2$. (d) A comparison of the extracted tunnel junction voltage drop for this work (shown as stars) as compared to other reported MOCVD (red) and MBE/hybrid (black) grown tunnel junctions. In this plot, empty shapes indicate all-GaN homojunction tunnel junctions, while solid shapes indicate heterojunction tunnel junctions.

The J–V characteristics for all structures grown are shown in Fig. 2(a). The reference p–n diode is the same in each structure, so the differences in voltage can be attributed to the different tunnel junction designs. Figure 2(b) shows the differential resistance vs current density curves for the various structures. To assess excess voltage penalty across each tunnel junction structure, the voltage drop across each structure is shown at current densities of 1 A/cm², 10 A/cm², and 100 A/cm² in Fig. 2(c). At an operating current density of 10 A/cm², compared to the Ohmic contact stand-alone p–n diodes (3.17 V @ 10 A/cm²), the graded InGa_N tunnel junctions (3.3 V @ 10 A/cm²) were able to reduce the voltage penalty to almost half that of the GaN homojunction tunnel junctions (3.46 V @ 10 A/cm²). The contacts to the reference p–n diode were Ohmic, which allowed for the p++Ga_N contact resistance to be de-embedded from the reference p–n diode characteristics for comparison purposes. To determine the tunnel junction voltage drop in the NPN structures, the voltage drop across the reference p–n diode was de-embedded by calculating the series resistance from the linear regime of the reference p–n diode J–V curve and extracting the intrinsic p–n diode characteristics. The tunnel junction-associated voltage drop was, then, compared to other results reported in the literature [Fig. 2(d)]. It can be seen that the graded InGa_N interlayer tunnel junctions exhibit a voltage drop of 0.17 V at 100 A/cm², which is the lowest reported to date for MOCVD-grown tunnel junctions. The GaN homojunction tunnel junction also achieved a voltage drop of 0.45 V at 100 A/cm², which is the lowest reported to date for an MOCVD-grown GaN homojunction. The tunnel junction voltage penalties obtained in this work offer a significant improvement upon previously reported values and are comparable with the lowest voltage drop MBE grown counterparts.^{24,28,35–37,42,43}

To explore the physical origin of the reduction in tunnel junction voltage drop observed in this work, simulations were developed using Silvaco TCAD. The material constants used in the simulations were taken from previously reported values.^{44,45} Nonlocal band-to-band tunneling models were used to account for tunneling within the tunnel junction. We included realistic MOCVD doping profiles obtained from the SIMS measurements shown in Fig. 1(d). We found that realistic MOCVD doping profiles within the tunnel junction give tunneling currents that are significantly different from idealized rectangular doping profiles. In the case of graded InGa_N layers, spontaneous and piezoelectric polarization constants used in the simulations followed Bernardini *et al.*⁴⁵ The impact of the thickness of the graded InGa_N layers within the tunnel junctions can be seen in Fig. 3(a). An optimal thickness of InGa_N offers a strong polarization induced field across a thin region within the tunnel junction, combined with a slightly lower energy barrier owing to the lower bandgap of InGa_N, leading to enhanced band-to-band tunneling rates.

To account for the effects of heavy magnesium doping within the p-type (In)Ga_N, band-tailing effects were also included in the simulation model. The bandgap narrowing due to band-tailing effects was calculated according to the universal bandgap narrowing model,⁴⁴

$$\Delta E_g = C \left[\frac{\epsilon_s^5}{N} \left(m_0 \frac{m_c + m_v}{m_c m_v} + B * T^2 \frac{\epsilon_s}{N} \right) \right]^{-\frac{1}{4}},$$

where N is the net doping density, m_c and m_v are the density of state effective masses for the conduction and valence bands, respectively, T is the temperature, and ε_s is the static dielectric constant. C and B are

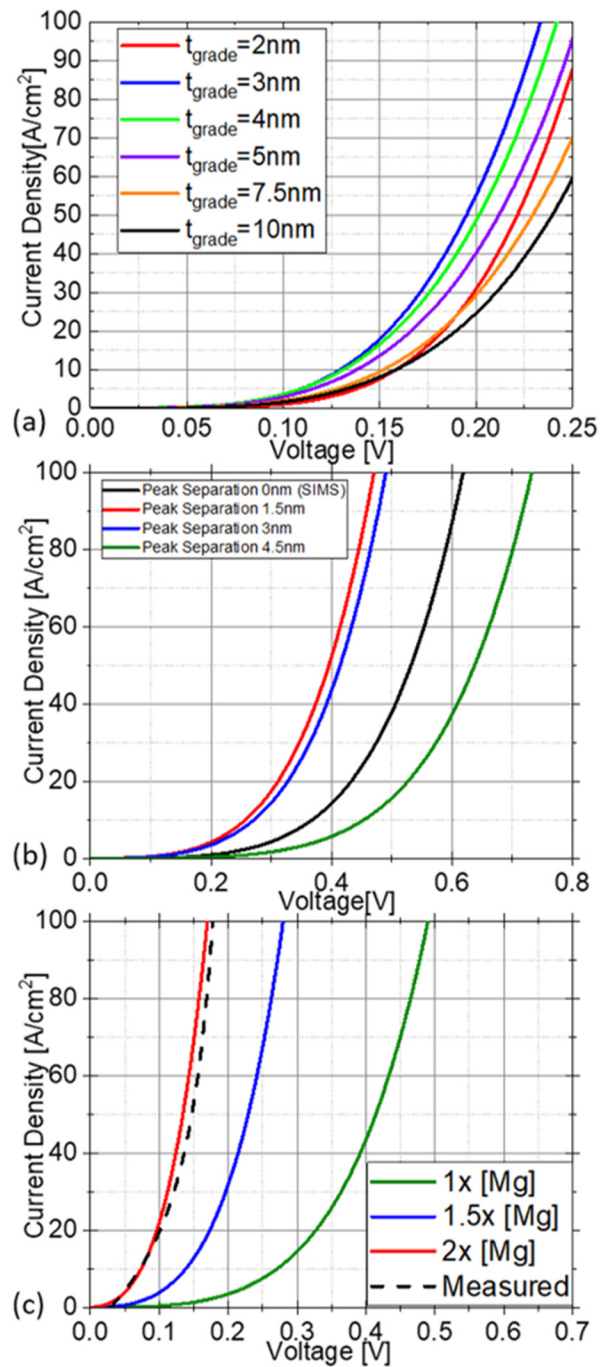


FIG. 3. (a) The simulated J–V characteristics for MOCVD grown graded InGa_N heterojunction tunnel junctions with graded layer thicknesses ranging from 2 nm to 10 nm. (b) The simulated J–V characteristics for doping peak separations ranging from 0 nm (defined as the measured SIMS profile) to 4.5 nm. (c) The simulated J–V characteristics for various peak [Mg] concentrations of 1.8 × 10²⁰ cm⁻³ (green), 2.65 × 10²⁰ cm⁻³ (blue), and 3.5 × 10²⁰ cm⁻³ (red) for a doping peak separation of 3 nm. The tunnel junction voltage drop de-embedded from the experimental measurement of the graded InGa_N tunnel junction structure is shown as a dashed line for comparison.

fitted parameters equal to $3.9 \times 10^{-5} \text{ eV/cm}^{3/4}$ and $3.1 \times 10^{12} \text{ cm}^{-3} \text{ K}^{-2}$, respectively. At the doping densities measured by SIMS, we estimated the bandgap energy to be 3.1 eV due to band-tailing effects at the location of peak net doping. In addition to a reduction in the bandgap, the band tailing also leads to an apparent decrease in the acceptor ionization energy, as reported previously for heavily Mg doped GaN.⁴⁶ With the reduced acceptor ionization energy included, the Mg acceptor ionization was estimated to be 50%. Inclusion of band-tailing effects in the simulation model led to a reduction in the simulated tunnel junction voltage drop; however, the values predicted were still higher than experimentally measured values. The SIMS measurements of Si and Mg were taken in different scans; therefore, the alignment of the peak locations in the SIMS measurement could differ slightly from the true doping profiles. To study the effect of peak separation between Si and Mg, simulations over the peak doping density locations were calculated. The location of the Si peak was fixed, and the Mg peak was separated by 1.5 nm, 3 nm, and 4.5 nm as shown in Fig. 2(b). It was determined that the simulated voltage drop across the tunnel junction was lower for the case of 1.5 nm and 3 nm as compared to the measured SIMS profiles. The experimentally measured voltage drop across the tunnel junctions was still considerably lower than the simulated values after including peak separation. To study the effect that laterally nonuniform of doping concentrations would have on the tunnel junction voltage penalty, another simulation was conducted by fixing the peak separation value, and then, sweeping the peak Mg doping concentration from $1 \times$ to $2 \times$, the value was measured by SIMS, from $[\text{Mg}] = 1.8 \times 10^{20} \text{ cm}^{-3}$ to $3.5 \times 10^{20} \text{ cm}^{-3}$. These simulated J-V curves for the case of 3 nm peak separation were compared with the tunnel junction voltage drop de-embedded from the experimental measurement of the graded InGaN interlayer tunnel junction as shown in Fig. 3(c). It can be seen that lateral nonuniformity in the doping profiles can lead to localized conduction paths with significantly lower resistance.

In summary, the work reported here demonstrates that it is possible to achieve low voltage losses across MOCVD-grown tunnel junction structures by understanding the origin of the excess voltage and designing the tunnel junctions to compensate for them. By including magnesium delta-dose doping in combination with graded InGaN interlayers, the voltage drop across the MOCVD-grown tunnel junction can be reduced significantly. We find that the voltage drop from experimental devices is significantly lower than the simulated values, which may be due to the growth inhomogeneity of doping profiles within the tunnel junction. The simulations suggest that inclusion of nonideal doping profiles, nonlocal tunneling, and band-tailing effects is critical to consider when designing MOCVD-grown tunnel junctions for low voltage drop. We can conclude that due to the high sensitivity of tunneling current to the doping profiles, more precise control and analysis of these at the nanometer scale is critical. The work reported here shows that MOCVD-grown tunnel junctions can be designed to provide ultralow voltage losses and enable many new device designs for III-nitride optoelectronic devices.

See the [supplementary material](#) (S1) for the Mg (black) and Si (red) doping concentrations as measured by SIMS for the graded InGaN heterojunction based tunnel junction and also the indium mole fraction (blue) measured by SIMS.

AUTHORS' CONTRIBUTIONS

Z.J.-E. and S.M.N.H. contributed equally to this work.

This material is based upon work supported by the U.S. Department of Energy's Office of Energy Efficiency and Renewable Energy (EERE) under the Building Technologies Office (BTO) Award No. 31150. Sandia National Laboratories is a multi-mission laboratory managed and operated by the National Technology and Engineering Solutions of Sandia, LLC., a wholly owned subsidiary of Honeywell International, Inc., for the U.S. Department of Energy's National Nuclear Security Administration under Contract No. DE-NA-0003525. The views expressed in the article do not necessarily represent the views of the U.S. Department of Energy or the U.S. Government.

DATA AVAILABILITY

The data that support the findings of this study are available from the corresponding author upon reasonable request.

REFERENCES

- ¹S.-R. Jeon, Y.-H. Song, H.-J. Jang, G. M. Yang, S. W. Hwang, and S. J. Son, *Appl. Phys. Lett.* **78**(21), 3265 (2001).
- ²M. Diagne, Y. He, H. Zhou, E. Makarona, A. V. Nurmikko, J. Han, K. E. Waldrip, J. J. Figiel, T. Takeuchi, and M. Krames, *Appl. Phys. Lett.* **79**(22), 3720 (2001).
- ³M. F. Schubert, *Appl. Phys. Lett.* **96**(3), 031102 (2010).
- ⁴Y. Zhang, S. Krishnamoorthy, J. M. Johnson, F. Akyol, A. Allerman, M. W. Moseley, A. Armstrong, J. Hwang, and S. Rajan, *Appl. Phys. Lett.* **106**(14), 141103 (2015).
- ⁵Y. Zhang, S. Krishnamoorthy, F. Akyol, S. Bajaj, A. A. Allerman, M. W. Moseley, A. M. Armstrong, and S. Rajan, *Appl. Phys. Lett.* **110**(20), 201102 (2017).
- ⁶Y. Zhang, Z. Jamal-Eddine, F. Akyol, S. Bajaj, J. M. Johnson, G. Calderon, A. A. Allerman, M. W. Moseley, A. M. Armstrong, J. Hwang, and S. Rajan, *Appl. Phys. Lett.* **112**(7), 071107 (2018).
- ⁷C. Kuhn, L. Sulmoni, M. Guttmann, J. Glaab, N. Susilo, T. Wernicke, M. Weyers, and M. Kneissl, *Photonics Res.* **7**(5), B7 (2019).
- ⁸F. Akyol, S. Krishnamoorthy, and S. Rajan, *Appl. Phys. Lett.* **103**(8), 081107 (2013).
- ⁹F. Akyol, S. Krishnamoorthy, Y. Zhang, and S. Rajan, *Appl. Phys. Express* **8**(8), 082103 (2015).
- ¹⁰S. Chang, W. Lin, and C. Yu, *IEEE Electron Device Lett.* **36**(4), 366 (2015).
- ¹¹S. Chang, W. Lin, and W. Chen, *IEEE J. Quantum Electron.* **51**(8), 3300505 (2015).
- ¹²J. Piprek, *Appl. Phys. Lett.* **104**(5), 051118 (2014).
- ¹³J. Piprek, *Phys. Status Solidi RRL* **8**, 424 (2014).
- ¹⁴C. H. Chen, S. J. Chang, Y. K. Su, J. K. Sheu, J. F. Chen, C. H. Kuo, and Y. C. Lin, *IEEE Photonics Technol. Lett.* **14**(7), 908 (2002).
- ¹⁵M. J. Grundmann and U. K. Mishra, *Phys. Status Solidi C* **4**(7), 2830 (2007).
- ¹⁶I. Ozden, E. Makarona, A. V. Nurmikko, T. Takeuchi, and M. Krames, *Appl. Phys. Lett.* **79**(16), 2532 (2001).
- ¹⁷B. P. Yonkee, E. C. Young, C. Lee, J. T. Leonard, S. P. DenBaars, J. S. Speck, and S. Nakamura, *Opt. Express* **24**(7), 7816 (2016).
- ¹⁸K. W. Hamdy, E. C. Young, A. I. Alhassan, D. L. Becerra, S. P. DenBaars, J. S. Speck, and S. Nakamura, *Opt. Express* **27**(6), 8327 (2019).
- ¹⁹S.-R. Jeon, C. S. Oh, J.-W. Yang, G. M. Yang, and B.-S. Yoo, *Appl. Phys. Lett.* **80**(11), 1933 (2002).
- ²⁰J. T. Leonard, E. C. Young, B. P. Yonkee, D. A. Cohen, T. Margalith, S. P. DenBaars, J. S. Speck, and S. Nakamura, *Appl. Phys. Lett.* **107**(9), 091105 (2015).
- ²¹S. Lee, C. A. Forman, C. Lee, J. Kearns, E. C. Young, J. T. Leonard, D. A. Cohen, J. S. Speck, S. Nakamura, and S. P. DenBaars, *Appl. Phys. Express* **11**(6), 062703 (2018).

- ²²M. Siekacz, G. Muziol, M. Hajdel, M. Żak, K. Nowakowski-Szkudlarek, H. Turski, M. Sawicka, P. Wolny, A. Feduniewicz-Żmuda, S. Stanczyk, J. Moneta, and C. Skierbiszewski, *Opt. Express* **27**(4), 5784 (2019).
- ²³J. Simon, Z. Zhang, K. Goodman, H. Xing, T. Kosel, P. Fay, and D. Jena, *Phys. Rev. Lett.* **103**(2), 026801 (2009).
- ²⁴S. Krishnamoorthy, P. S. Park, and S. Rajan, *Appl. Phys. Lett.* **99**(23), 233504 (2011).
- ²⁵A. T. M. G. Sarwar, B. J. May, J. I. Deitz, T. J. Grassman, D. W. McComb, and R. C. Myers, *Appl. Phys. Lett.* **107**(10), 101103 (2015).
- ²⁶X. Yan, W. Li, S. M. Islam, K. Pourang, H. Xing, P. Fay, and D. Jena, *Appl. Phys. Lett.* **107**(16), 163504 (2015).
- ²⁷E. A. Clinton, E. Vadiie, S.-C. Shen, K. Mehta, P. D. Yoder, and W. A. Doolittle, *Appl. Phys. Lett.* **112**(25), 252103 (2018).
- ²⁸M. Kaga, T. Morita, Y. Kuwano, K. Yamashita, K. Yagi, M. Iwaya, T. Takeuchi, S. Kamiyama, and I. Akasaki, *Jpn. J. Appl. Phys., Part 1* **52**(8S), 08JH06 (2013).
- ²⁹D. Hwang, A. J. Mughal, M. S. Wong, A. I. Alhassan, S. Nakamura, and S. P. DenBaars, *Appl. Phys. Express* **11**(1), 012102 (2018).
- ³⁰S. Neugebauer, M. P. Hoffmann, H. Witte, J. Blasing, A. Dadgar, A. Strittmatter, T. Niermann, M. Narodovitch, and M. Lehmann, *Appl. Phys. Lett.* **110**(10), 102104 (2017).
- ³¹P. Sohi, M. Mosca, Y. Chen, J.-F. Carlin, and N. Grandjean, *Semicond. Sci. Technol.* **34**, 015002 (2019).
- ³²Y. Akatsuka, S. Iwayama, T. Takeuchi, S. Kamiyama, M. Iwaya, and I. Akasaki, *Appl. Phys. Express* **12**(2), 025502 (2019).
- ³³V. F. Arcara, B. Damilano, G. Feuillet, A. Courville, S. Chenot, and J.-Y. Duboz, *AIP Adv.* **9**(5), 055101 (2019).
- ³⁴A. J. Mughal, E. C. Young, A. I. Alhassan, J. Back, S. Nakamura, J. S. Speck, and S. P. DenBaars, *Appl. Phys. Express* **10**(12), 121006 (2017).
- ³⁵S. Krishnamoorthy, F. Akyol, P. S. Park, and S. Rajan, *Appl. Phys. Lett.* **102**(11), 113503 (2013).
- ³⁶S. Krishnamoorthy, D. N. Nath, F. Akyol, P. S. Park, M. Esposto, and S. Rajan, *Appl. Phys. Lett.* **97**(20), 203502 (2010).
- ³⁷S. Krishnamoorthy, F. Akyol, and S. Rajan, *Appl. Phys. Lett.* **105**(14), 141104 (2014).
- ³⁸F. Akyol, S. Krishnamoorthy, Y. Zhang, J. Johnson, J. Hwang, and S. Rajan, *Appl. Phys. Lett.* **108**(13), 131103 (2016).
- ³⁹E. Vadiie, E. A. Clinton, J. V. Carpenter, H. McFavlen, C. Arena, Z. C. Holman, C. B. Honsberg, and W. A. Doolittle, *J. Appl. Phys.* **126**(8), 083110 (2019).
- ⁴⁰S. M. N. Hasan, B. P. Gunning, Z. Jamal-Eddine, H. Chandrasekar, M. H. Crawford, A. Armstrong, S. Rajan, and S. Arafin, *arXiv:2011.13431* (2020).
- ⁴¹D. Takasuka, Y. Akatsuka, M. Ino, N. Koide, T. Takeuchi, M. Iwaya, S. Kamiyama, and I. Akasaki, *Appl. Phys. Express* **9**(8), 081005 (2016).
- ⁴²D. Minamikawa, M. Ino, S. Kawai, T. Takeuchi, S. Kamiyama, M. Iwaya, and I. Akasaki, *Phys. Status Solidi B* **252**(5), 1127 (2015).
- ⁴³Z.-H. Zhang, S. T. Tan, Z. Kyaw, Y. Ji, W. Liu, Z. Ju, N. Hasanov, X. W. Sun, and H. V. Demir, *Appl. Phys. Lett.* **102**(19), 193508 (2013).
- ⁴⁴J. Piprek, *Semiconductor Optoelectronic Devices: Introduction to Physics and Simulation* (Elsevier, 2013).
- ⁴⁵F. Bernardini, V. Fiorentini, and D. Vanderbilt, *Phys. Rev. B* **56**(16), R10024 (1997).
- ⁴⁶B. Gunning, J. Lowder, M. Moseley, and W. A. Doolittle, *Appl. Phys. Lett.* **101**(8), 082106 (2012).